Journal of Manufacturing Processes 93 (2023) 299–314

Contents lists available at ScienceDirect

Journal of Manufacturing Processes

journal homepage: www.elsevier.com/locate/manpro

A finite difference method for fast prediction and control of part-scale temperature evolution in laser powder bed fusion

Yong Ren, Qian Wang *

Department of Mechanical Engineering, The Pennsylvania State University, University Park, PA 16802, United States of America

ARTICLE INFO

Keywords:
Part-scale thermal modeling
Interlayer temperature
Finite difference method
Optimal control of laser power
Temperature evolution

ABSTRACT

Part-scale thermal modeling is a crucial building block in the multi-scale thermo-mechanical analysis for laser powder bed fusion process, and it plays a pivotal role in enabling computationally efficient thermal simulation of parts of large size. This paper presents a novel finite difference model that can provide fast prediction of part-scale temperature evolution to enable model-based part-scale thermal control. The effectiveness of the proposed modeling method is illustrated through a case study of a square-canonical geometry of Inconel 718, where several heat transfer parameters of the model are identified by matching the model computation with the in-situ measurements of interlayer temperature obtained from the build process on an EOS M280 system. The root-mean-square error between the model computed interlayer temperature and mean values of the measured temperature is less than 25 °C, suggesting that the model captures the major underlying physics for interlayer temperature prediction once the model parameters are identified. The proposed modeling efforts demonstrate that the heat transfer between part components and powder bed is essential to characterize part-scale temperature evolution. Based on the proposed part-scale thermal model, a numerical study on optimal control of interlayer temperature through layer-by-layer control of laser power is also presented. Results from this study set a foundation for future experimental investigation of model-based part-scale thermal control to reduce overheating by which to improve build quality for powder bed fusion systems.

1. Introduction

Laser powder bed fusion (L-PBF) processes are one important subcategory of metal additive manufacturing (AM) processes, which enable fabrication of complex parts with high geometric resolution, and nearly full part density, with wide applications in medical, aerospace, and automotive industries [1,2]. The underlying physics of the L-PBF process is complicated and operates over different time and length scales [3,4]. For example, the laser beam diameter size and the powder layer thickness are at the order of tens of microns, while the final parts could be on the order of cubic centimeters in dimension. The laser speed could range from a few hundred to thousand millimeter-per-second, while the build times could last hours and days. Therefore, it calls for multiscale modeling ranging from powder-scale to part-scale simulations.

To represent powder particles, powder-scale models typically require a mesh size on the order of microns, by which mesoscopic models have been developed to simulate laser-powder interaction including powder melting, hydrodynamic effects, and formation mechanism of pores, spatter and denudation [5–11]. However, the associated high computational cost often limit the powder-scale models to simulating the melting process of a single-line, in the range of multiple-hundred micrometers to millimeters, or up to a few layers with equivalent-scale dimensions [3,12]. By approximating the powder bed as a continuum rather than particles, the continuum approaches to modeling have significantly reduced computation demand through coarsening the spatial and temporal resolution. Along this direction, moving-source models, based on finite element methods (FEM) or finite volume methods (FVM), have been developed to investigate the effect of heat source parameters and scan path on the melt-pool geometry and fluid dynamics [13–19], as well as on temperature distribution and stress field [20–25].

Part-scale simulations often refer to the computational domain size at the order of 10 cm × 10 cm × 10 cm [26], for which the computation cost of moving-source models is still too high to be applied efficiently [27]. Consequently, part-scale models have emerged to focus on the aggregate effect of the process on the temperature field evolution

* Corresponding author.
E-mail address: quw6@psu.edu (Q. Wang).

https://doi.org/10.1016/j.jmapro.2023.03.020
Received 29 November 2022; Received in revised form 11 February 2023; Accepted 11 March 2023

[28–31], residual stress and part distortion [32–35] by omitting the details of the local laser-powder interaction and melt-pool dynamics. It is assumed that the heating process of a whole layer of the powder bed by the laser beam is simultaneous. Consequently, hatch-by-hatch scanning strategies are not explicitly accounted in the part-scale models.

In addition, layer-scaling is commonly employed by part-scale modeling to further reduce computation cost [33,36–38], where deposition of multiple physical layers is simulated by depositing a grouped layer. The computation efficiency of part-scale, FEM models for L-PBF could be further increased through a graphical processing unit (GPU) implementation [26]. A few studies also demonstrated mesh-free models for L-PBF. Yavari et al. developed a mesh-free, graph-theory based approach to predict temperature distribution [39] by utilizing the eigenvector and eigenvalues of the graph Laplacian. A thermal circuit network model was developed by Peng et al. [40], where each grouped layer was divided into multiple thermal circuit elements consisting of thermal capacitors and resistors.

In this paper, we present a finite-difference method (FDM) for quick prediction of part-scale thermal evolution with the objective of enabling a model-based part-level optimization of process parameters to reduce the risk of overheating in the build process. For modeling of AM processes, FDM was often limited to simple geometries. For example, Ganeriwala and Zohdi used FDM to model heat conduction in a rectangular shaped substrate underneath powder particles for a selective laser sintering process [41]. McMillan et al. applied FDM to model 1-D heat conduction in lattice structures, used as a design-for-AM tool [42]. The FDM proposed in this study differentiates from the work by McMillan et al. [42] in several aspects: (1) it models part-scale thermal evolution rather than focusing on fine-scale simulations as in [42]; (2) it includes powder and support-structure elements in the thermal modeling, and by including the powder and support elements, the network flow is not restricted to 1D as in [42] anymore; and (3) it is demonstrated for a convex optimization of process parameters for part-scale thermal control.

In this paper, we are particularly interested in the modeling and subsequent model-based control of *interlayer temperature* right before scanning each new layer. Interlayer temperature refers to the layer temperature after the powder is spread but before scanning a new layer commences. It represents the part heating due to the processing of the previous layers, and it acts as the initial temperature under which a new layer is scanned [35]. Promoppatum et al. showed that interlayer temperature has a significant impact to the melt-pool morphology and microstructure [43]. Chen et al. showed that under EOS M290's default process parameters, the melt-pool depth of single-scan tracks increased by 31% when the initial (preheating) temperature increased from 100 °C to 500 °C, where the melt-pool morphology falls in the transitional regime to keyholing [44]. Tran et al. showed that when the surface temperature of the previous layer increased from 80 °C to 400 °C, a significantly broader range of laser power (P) and scan velocity (V) combination in the P-V map would lead to keyhole melting [45]. These studies have motivated us to control interlayer temperature by varying process parameters layer-by-layer. To enable the design of a model-based control, an FDM is proposed in this study to provide quick prediction of part-level temperature evolution.

The paper is organized as follows. Section 2 introduces the basic equations for transient heat transfer and assumptions. Section 3 shows the FDM for a 1D problem, in comparison to an analytical heat transfer calculation in the layer-by-layer building of an 1-D rod. Section 4 illustrates the FDM for a 3D part through a case study of a square-canonical geometry, where several heat transfer parameters of the model are identified (calibrated) by matching the FDM computation with the in-situ measurements of interlayer temperature. Section 5 presents a part-level thermal optimization to illustrate that the proposed FDM could be used to derive the layer-by-layer laser power profiles to control interlayer temperature. Section 6 discusses the runtime of the modeling and process optimization and its implication towards real-time implementation. Conclusions are drawn in the end.

2. Transient heat transfer and assumptions

In this paper, it is assumed that the thermal properties of all materials are constant, as conducted in the part-scale finite-element based thermal models [46] to simplify the process physics. The transient heat conduction can be described by the following equation for the temperature $T(x, y, z; t)$:

$$\rho c_p \frac{\partial T}{\partial t} = \nabla \cdot \mathbf{q}(x, y, z; t) + Q(x, y, z; t) \tag{1}$$

where $\mathbf{q}$ denotes the heat flux satisfying

$$\mathbf{q} = -\kappa \nabla T \tag{2}$$

ρ, c_p, and κ denote the material density, specific heat, and conductivity respectively; and Q denotes the volumetric heat source to account for laser heating.

The convective heat loss q_{conv} satisfies

$$q_{conv} = h(T_s - T_a) \tag{3}$$

where h is the convection coefficient, T_s is the surface temperature and T_a is the ambient temperature.

The heat loss due to radiation is omitted here. Assuming constant thermal properties and omitting heat loss due to radiation render the resulting transient heat transfer model to be linear. This paper is aimed to derive part-scale thermal models, where the heating process of a whole layer of the powder bed by the laser beam is assumed to be simultaneous. In the FEM part-scale thermal analysis conducted by Li et al. [47], the energy of laser melting applied to each layer can be alternatively modeled by activating each layer at an elevated initial temperature, referred to as the activation temperature T_{act}:

$$T_{act} = T_a + \frac{\eta P}{\rho c_p l_{hs} t_\theta v}. \tag{4}$$

where η is the laser absorption efficiency, P is the laser power, l_{hs} denotes the hatch spacing, t_θ is the thickness of each physical layer, and v is the laser scan speed. Noting that the energy density can be computed as $E = \eta P/(l_{hs} t_\theta v)$ [48], the second term in the right hand side of Eq. (4) can be written as $E/(\rho c_p)$, equivalent to the temperature increase caused by laser irradiation of a unit mass. The activation temperature T_{act} here imitates the impulse input numerically, i.e., it has a very high magnitude with the time duration approaching zero.

Consequently, rather than solving the moving heat source problem with respect to Q in Eq. (1), the following heat diffusion problem is considered in a layer-by-layer manner:

$$\frac{\partial T}{\partial t} = \alpha \nabla^2 T \tag{5}$$

$$T(x, y, z; t_0) = T_{act} \quad on \quad \Gamma_{ir} \tag{6}$$

where α is the thermal diffusivity satisfying $\alpha = \kappa/(\rho C_p)$, and Γ_{ir} represents the top layer where the laser irradiation is applied.

In Section 3, FDM is first illustrated to solve (5)–(6) for a 1D problem and compared to the analytical solution. For a 3D part, discretizing Eq. (5) over a generic uniform grid to derive a finite difference model can be found in a textbook [49] and is not adopted in this paper. Instead, for a 3D part built layer-by-layer where each layer consists of multiple disjointed part components, we define a node for each disjointed component in the layer regardless of the shape of the component (see Section 4). The corresponding nodal temperature represents the average surface temperature of that disjointed component. Consequently, the proposed FDM models a part fabrication as a multi-branch network along the build direction. Such modeling allows improved computation efficiency than using a regular grid at the cost of computation accuracy.

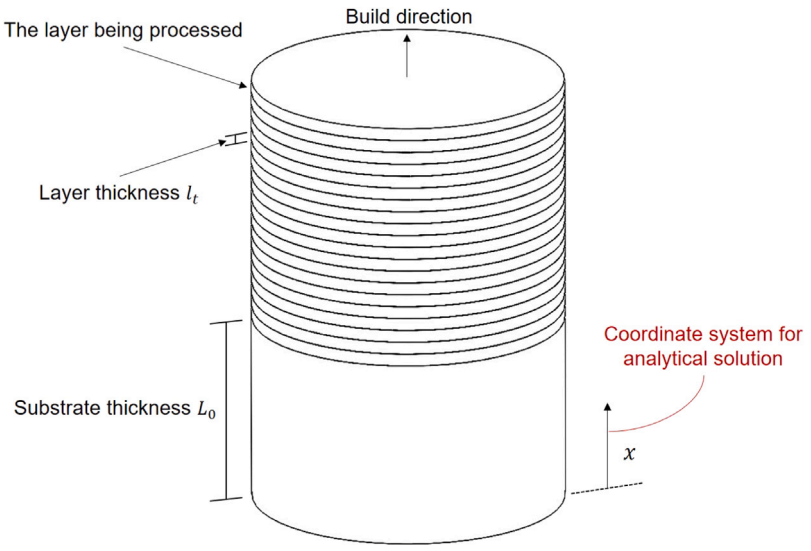

Fig. 1. 1-D rod-substrate ensemble.

3. 1-D model and numerical verification

3.1. 1-D heat conduction and solution

Consider the 1-D problem defined in Fig. 1, where the laser melts a sequence of layers of a rod with identical cross-sectional area along the build direction. For simplicity, assume that both ends of the rod-substrate ensemble are insulated, i.e., no convection is considered. Let L_0 denote the substrate thickness, and l_t denote the thickness of each (grouped) layer. It is assumed that the substrate has the same material and cross-sectional area as the part. Let t_j $(j = 1, 2, \ldots)$ denote the time instant right before the laser starts to melt the jth-layer, and let t_{tot} denote the summation of laser processing time t_{proc} and recoating time t_{recoat}. Then $t_{tot} = t_{proc} + t_{recoat}$, and $t_{j+1} = t_j + t_{tot}$.

1. Consider the first layer $j = 1$. At $t = t_1$, the first layer of powder has already been laid on the substrate. Recall that the heat flux due to the laser power acting on the top layer of powder can be replaced by an activation temperature T_{act} in Eq. (4). Consider the temperature $T(x, t)$ at any location $x \in [0, L_1]$ with $L_1 = L_0 + l_t$ and $t \in [t_1, t_2)$. Further define $t' = t - t_1$, then $T(x, t')$ satisfies the following heat conduction equation:

$$\frac{\partial T}{\partial t'} = \alpha \frac{\partial^2 T}{\partial x^2} \tag{7}$$

with initial condition:

$$T(x, t' = 0) = \begin{cases} T_a, & 0 \le x < L_0 \\ T_{act}, & L_0 \le x < L_1 \end{cases} \tag{8}$$

and the Neumann boundary conditions:

$$\frac{\partial T}{\partial x}(0, t') = \frac{\partial T}{\partial x}(L_1, t') = 0 \tag{9}$$

The solution to the heat conduction in Eq. (7)–Eq. (9) can be easily derived (see Appendix A for details). Let $T^{(1)}(x, t')$ denote the corresponding solution, with $x \in [0, L_1]$, and $t' \in [0, t_{tot}]$. Note that the temperature distribution $T^{(1)}(x \in [0, L_1], t' = t_{tot})$ serves as the initial condition when the laser starts to melt the 2nd-layer of material at $t = t_2$.

2. Consider a general layer $j > 1$. Define $t' = t - t_j$, then the temperature distribution is governed by the same heat conduction Eq. (7), subject to the boundary conditions:

$$\frac{\partial T}{\partial x}(0, t') = \frac{\partial T}{\partial x}(L_j, t') = 0 \tag{10}$$

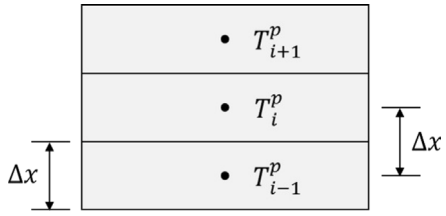

Fig. 2. Three adjacent elements with nodal temperature T and nodal spacing Δx.

where $L_j = L_0 + j \times l_t$. The initial conditions can be written as

$$T(x, t' = 0) = \begin{cases} T^{(j-1)}(x, t_{tot}), & x \in [0, L_{j-1}) \\ T_{act}, & x \in [L_{j-1}, L_j] \end{cases} \tag{11}$$

By the technique of separation of variables [50], the solution of the temperature distribution can be expressed as follows:

$$T^{(j)}(x, t') = \frac{c_0^{(j)}}{2} + \sum_{k=1}^{\infty} c_k^{(j)} e^{-\alpha(\frac{k\pi}{L_j})^2 t'} \cos(\frac{k\pi x}{L_j}). \tag{12}$$

for $x \in [0, L_j]$ and $t' \in [0, t_{tot}]$. The coefficients $c_0^{(j)}$ and $c_k^{(j)}$ can be computed using the initial condition in Eq. (11) with details given in Appendix A.

3.2. Finite-difference model and verification

An implicit-form, finite-difference model for the 1D problem can be obtained by discretizing Eq. (7) in time along the build direction. One element is assigned to each layer of the rod. Assume that the substrate is partitioned into N_s elements and each substrate element has the same thickness as each rod element, i.e., $L_0 = N_s \cdot l_t$ (see Fig. 1).

Consider that rod layer j is under melting, where $t_j \le t \le t_{j+1}$. During this time period, the rod-substrate ensemble contains a total of N_j elements with $N_j = N_s + j$. Let Δt denote the sampling time, and let T_i^p denote the nodal temperature of an element i at time iteration p, with the nodal spacing $\Delta x = l_t$ (see Fig. 2). For elements $i = 2, \ldots, N_j - 1$, discretizing Eq. (7) leads to the following:

$$\frac{T_i^{p+1} - T_i^p}{\Delta t} = \frac{\alpha}{\Delta x^2}(T_{i-1}^{p+1} - 2T_i^{p+1} + T_{i+1}^{p+1}) \tag{13}$$

Table 1
Simulation parameters for the 1D problem, where material properties are for Inconel 718.

Parameter	Value	Unit
P	285	W
η	0.4	–
v	960	mm/s
T_a	25	°C
α	3.2774	mm^2/s
ρ	8.146×10^{-6}	kg/mm^3
c_p	427	J/kg K
l_{hs}	0.11	mm
t_θ	0.04	mm
$\Delta x = l_t$	1	mm
L_0	30	mm
t_{tot}	30	s
Δt	1	s
N_s	30	–

For $i = 1$, which represents the bottom element of the substrate,

$$\frac{T_1^{p+1} - T_1^p}{\Delta t} = \frac{\alpha}{\Delta x^2}(T_2^{p+1} - T_1^{p+1}) \tag{14}$$

and for $i = N_j$, which denotes the element representing the top melting layer,

$$\frac{T_{N_j}^{p+1} - T_{N_j}^p}{\Delta t} = \frac{\alpha}{\Delta x^2}(T_{N_j-1}^{p+1} - T_{N_j}^{p+1}) \tag{15}$$

The initial conditions in Eqs. (8) and (11) can be defined accordingly.

Further define the temperature vector $\mathbf{T}^p = [T_1^p, \ldots, T_{N_j}^p]^\top$ with $[\cdot]^\top$ denoting vector transpose, and define

$$\mathbf{M} = \mathbf{I} + \frac{\alpha\Delta t}{\Delta x^2} \times \begin{bmatrix} 1 & -1 & 0 & 0 & \cdots & 0 \\ -1 & 2 & -1 & 0 & \cdots & 0 \\ 0 & -1 & 2 & -1 & \cdots & 0 \\ \vdots & \vdots & \vdots & \ddots & \vdots & \vdots \\ 0 & 0 & 0 & \cdots & 2 & -1 \\ 0 & 0 & 0 & \cdots & -1 & 1 \end{bmatrix}, \tag{16}$$

where $\mathbf{I}$ denotes an identical matrix with dimension $N_j \times N_j$. Then, the finite-difference model in Eq. (13)–Eq. (15) can be rewritten in the following compact form:

$$\mathbf{T}^{p+1} = \mathbf{M}^{-1}\mathbf{T}^p. \tag{17}$$

Fig. 3 shows a comparison of the finite-difference model predicted temperature versus the analytical solution in Eq. (12) during the first three layers of the rod-substrate ensemble. The parameter values used for the computation are given in Table 1. Noting that the analytical solution in Eq. (12) and the coefficients $c_k^{(j)}$ (see Appendix A) contain infinite series, only the first 30 terms of any infinite series are included in computation for comparison shown in Fig. 3. In Fig. 3(a), the temperature history at $x = 30.5$ mm (center point of the first layer) from each method is plotted. The discrepancy between the FDM computed temperature and the analytical solution could be partially attributed to (i) that only a finite number of terms are used in computing the Fourier series, and (ii) discontinuity of the initial condition in Eq. (11) caused from scanning a new layer, where the Gibbs phenomenon can be observed when a Fourier series expansion is used to express the initial condition. Fig. 3(b) plots the temperature distribution with respect to x right before scanning the 2nd layer (at $t = 30$ s), the 3rd layer ($t = 60$ s), and the 4th layer ($t = 90$ s). The last data point of each of the three temperature curves constitutes the interlayer temperature for the first three layers. Overall, Fig. 3 shows that the computation from the FDM has a good agreement with the analytical solution for the 1D problem.

4. 3-D model for a square-canonical geometry

This section illustrates how the proposed FDM is applied to compute part-scale thermal evolution for a 3D part, where a square-canonical geometry is used as a case study. Several heat transfer parameters of the model are identified by matching the model computation with the in-situ measurements of interlayer temperature obtained through thermographic imaging during the build process from our prior work [51].

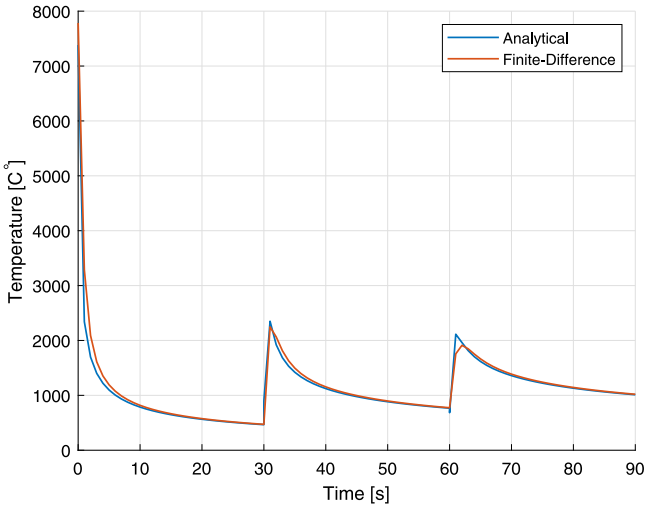

(a)

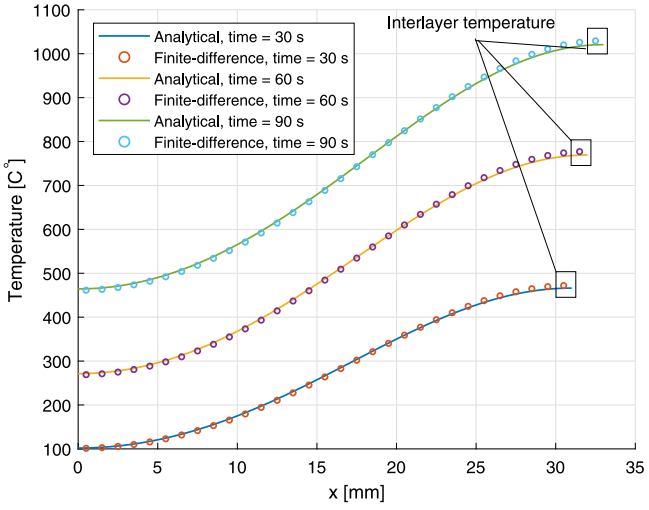

(b)

Fig. 3. Comparison of finite-difference model computation and analytical solution. (a) Temperature history at $x = 30.5$ mm; (b) Temperature distribution of the rod-substrate ensemble at the time instant $t = 30$ s (right before scanning the 2nd layer), $t = 60$ s (right before 3rd layer), and $t = 90$ s (right before 4th layer).

4.1. A square-canonical geometry

The square-canonical geometry shown in Fig. 4 was originally designed by the America Makes Project No. 4026 for the purpose of validating thermo-mechanical models for L-PBF [52]. It is chosen here as a case study for part-level thermal modeling due to its geometric features to create overheating, and thus, it could serve as a candidate for part-level thermal control. The square of the canonical part has a dimension of 64.24 mm × 64.24 mm, and the part has 1270 layers with

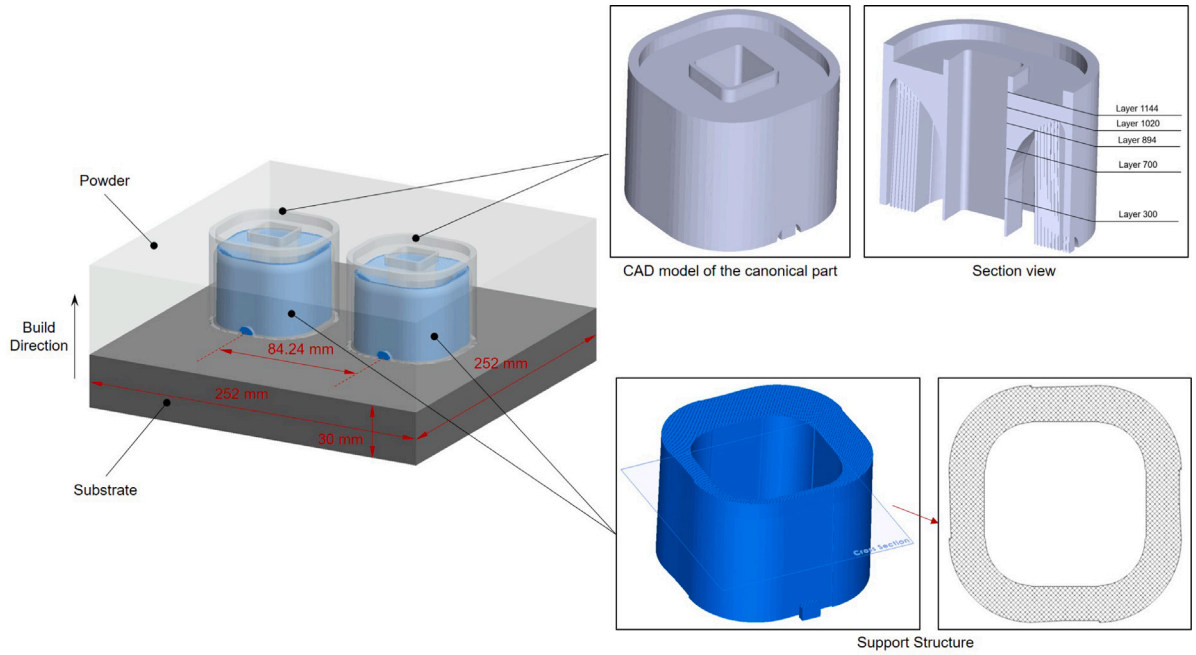

Fig. 4. Two identical square-canonical geometry of Inconel 718 built at the center of a substrate of tool steel with a dimension of 252 mm × 252 mm × 30 mm.

Table 2
Experimental process parameters used for fabricating the canonical parts.

Parameter	Value	Unit
Recoating time	8.5	s
Laser power (part)	285	W
Laser power (support structure)	100	W
Laser transmission efficiency	0.4	
Laser scan speed (part)	960	mm/s
Laser scan speed (support structure)	900	mm/s
Ambient temperature	25	°C
Substrate preheating temperature	80	°C
Hatch space	0.11	mm
Physical layer thickness	0.04	mm
Substrate thickness	30	mm
Support (solid) volume fraction	0.27	–

a total height of 50.8 mm. It consists of an inner wall and an outer wall. The two walls are separated at lower layers, where the thickness of the inner wall is 0.83 mm and the thickness of the outer wall is 2.29 mm. The width of the inner wall increases with the increase of the layer number and eventually it merges with the outer wall as a single junction, which later splits again. It is expected that with the growth of the mass of the inner wall, heat is accumulated but there is a lack of sufficient conduction path to transfer heat into the substrate, causing overheating.

Two identical square-canonical parts of Inconel 718 were built on a tool steel substrate of 252 mm × 252 mm × 30 mm using the EOS M280 L-PBF system. The bottom center of the substrate is heated and maintained at a constant 80 °C during the build process. The process parameters used for fabrication are given in Table 2. Support structures of Inconel 718 are used to build the small arch (small arch support) at the lower-level of the geometry and to build the overhang connecting the inner and outer walls (main support). The support cross-section is composed of square honeycomb with wall spacing of 0.82 mm and wall thickness of 0.12 mm, leading to a volume fraction (ratio of solid-component volume over the entire support volume) of $v = 0.27$. In-situ thermographic measurements of interlayer temperature distribution were captured using a midwave IR camera during the build process, for which readers are referred to [51] for details. Interlayer temperature distributions at selected physical layers are given in Appendix B.

4.2. Finite difference model

FDM is the most direct approach to discretizing partial differential equations, and it is typically defined on a regular grid. To model the interlayer temperature evolution, rather than considering a regular grid as in Fig. 5 (left), this paper defines a node for each disjointed component in a part slice. As illustrated in Fig. 5 (right), for a part slice, a node is defined for the outer-wall component, a node for the inner-wall component, a node for the support structure, and an aggregate node is defined to represent the powder that is connected to all other nodes (i.e., interacting with other parts) in the same slice. Compared to using a regular grid, the proposed nodal definition and resulting nodal network allow a much easier way to handle curved or irregular geometries such as the square-canonical geometry, which is a great advantage. Using a single node to represent the interlayer temperature for each disjoint component in a part slice of the canonical geometry leverages the observation that the variance of the interlayer-temperature distribution of each disjoint component is small, as shown later in Section 4.3. The experimental data in Section 4.3 also show that the small variance in interlayer temperature is not necessarily limited to the thin-wall features of the geometry, as it remains small during the layers where the single junction merging the inner- and outer-walls is built. When the variance of interlayer-temperature distribution of each disjointed component is substantial, more nodes could be needed for each disjointed component in a layer to reflect the variability in temperature distribution.

4.2.1. Multi-branch network

Layer-scaling is used in the proposed FDM for the square-canonical geometry, where a grouped part layer is defined to consist of 18 physical layers in this study. For finite-element based part-scale models, a numerical layer representing 10–20 physical layers, with a physical layer of 40–50 μm, was commonly used in the literature [26,37]. In terms of experimental measurements [51], the standard deviation of mean interlayer temperature across the 18 physical layers of each grouped layer is less than 10 °C.

Corresponding to a physical layer of 40 μm, the thickness of a grouped layer is 0.72 mm and the part is sliced into a total of $N_{layers} = 70$ grouped layers. In the remainder of this paper, *a layer* is used to

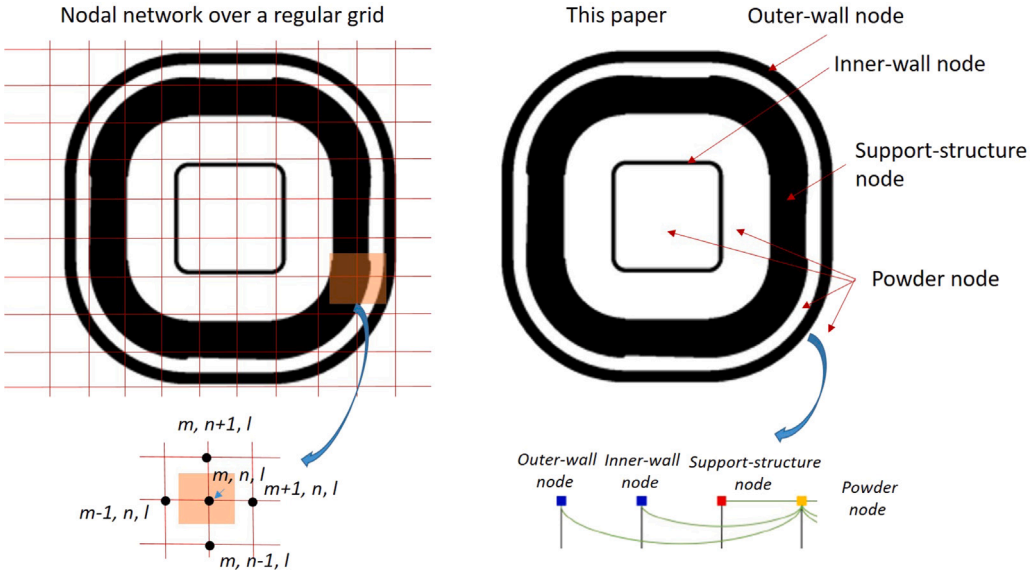

Fig. 5. Illustration for a part slice: comparison of nodal network over a conventional regular grid versus nodal network defined in this paper.

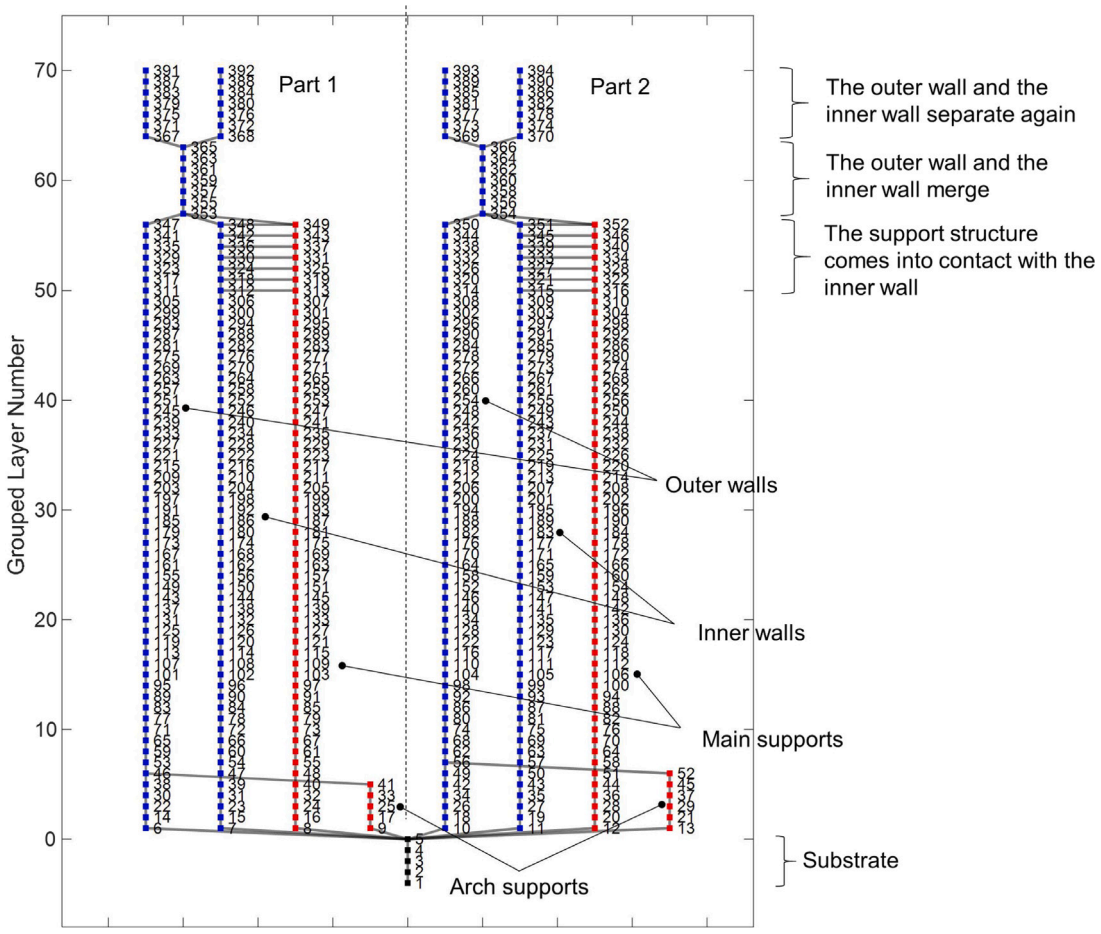

Fig. 6. A multi-branch network showing thermal conduction among the elements used in the finite-difference model, where black nodes are for substrate, blue nodes for part components, and red nodes for support structures; powder nodes are not shown here. (For interpretation of the references to color in this figure legend, the reader is referred to the web version of this article.)

refer to a grouped layer for simplicity unless explicitly noted to be a *physical* layer. Fig. 6 shows the multi-branch network modeled for the two identical canonical parts (Part 1 and Part 2) built on a single substrate. Specifically,

- Substrate: the substrate is partitioned into N_s layers and a node is defined for each layer. $N_s = 5$ is chosen here, by which the distance between two substrate nodes is 6 mm. In Fig. 6, the first 5 nodes below the first part layer correspond to the substrate nodes.

- When the inner and outer walls are separate (layer No. ≤ 56): at each layer of a part, one node is defined for the inner wall, and one for the outer wall. In addition, one node is defined for each support structure in a layer that has support structure(s).
- When inner and outer walls are merged into a single junction (layer No. 57–63) : only one node is defined for each layer of a part.
- When inner and outer walls separate again (layer No. 64–70): for each layer of a part, one node is defined for the inner wall and one node for the outer wall.

Each edge linking two nodes represents that the two nodes have surface contact and there is thermal conduction between the two nodes. For example, there is conduction between any two adjacent layers of inner wall, same for the outer wall, the substrate, and each support. As a result, along the build direction, multiple branches have formed for each canonical part, including the inner-wall branch, outer-wall branch, arch-support branch and main-support branch. In the multi-branch network, a node could be connected (in contact) to multiple nodes, leading to splitting heat flow rate from one node to multiple nodes or merging heat flow rate from multiple nodes to a single node. For example, the top node of the substrate is connected to all nodes in the first layer, as both canonical parts and their support structures are built on top of the substrate. The top node of the small arch support is connected to the outer wall. At layer No. 50–56, the main support is in contact with the inner wall (see section view of the part at the physical layers 894–1020 in Fig. 4) and thus there is an edge linking each main-support node to the corresponding inner-wall node in the same layer. That is, there is heat conduction along the horizontal edges in addition to the heat conduction going down the build. The last node of the main support is then connected to the first node of the single junction where the two walls merge.

Case I: No powder elements. Dugast et al. assumed that the heat convection at the part and powder interface equals zero in their simulation model [26]. Li et al. investigated two finite-element simulation models: one with both the part and powder elements, whereas the other included only the part elements. Then, the convection coefficients at the boundary conditions of the no-powder model were estimated to match the simulation results of the model with powder elements [47]. Following the no-powder approach in [47], powder elements are not defined in Case I, but instead, the surface convection coefficients at the boundary conditions are identified using experimental data to estimate the heat loss from the solid components to the surrounding powder.

Consider that layer ℓ is under processing in Fig. 6, for any node i and time increment p, the temperature T_i^p satisfies the following energy balance equation:

$$\underbrace{\frac{A_{cs}^i \rho_i c_{p,i} \Delta x_i}{\Delta t}(T_i^{p+1} - T_i^p)}_{\text{Rate of energy change}} = \underbrace{\sum_{j \in \mathcal{N}_i^\ell} \frac{A_{ol}^{i,j} \kappa_{i,j}}{\delta_{i,j}}(T_j^{p+1} - T_i^{p+1})}_{\text{Conduction}} + \underbrace{A_{sf}^i h_i (T_a - T_i^{p+1})}_{\text{Convection on surfaces}} \tag{18}$$

- The left-hand-side (LHS) term computes the rate of energy stored in node i, where A_{cs}^i denotes its cross-sectional area and Δx_i denotes the thickness of the element; ρ_i is its density, and $c_{p,i}$ denotes its specific heat.
- The first right-hand-side (RHS) term computes the summation of conductive heat loss to its neighboring elements $\{j | j \in \mathcal{N}_i^\ell\}$, where $A_{ol}^{i,j}$ denotes the overlap (contacting) area between node i and its neighboring node j; $\kappa_{i,j}$ denotes the thermal conductivity between node i and node j. When the two nodes are of different materials, $\kappa_{i,j}$ represents an equivalent conductivity to compute the conduction heat loss; $\delta_{i,j}$ denotes the distance between the centers of the two nodes i and j.
- The second RHS term computes the convective heat loss to the air or powder, where A_{sf}^i denotes the surface area of node i exposed to air or powder, and h_i denotes the surface convection coefficient.

Fig. 7(a) illustrates the types of elements involved (part/substrate/support for Case I) and thermal conductivity between any two elements. The thermal conductivity between any i and j, $\kappa_{i,j}$, can be classified into $\kappa_{A,B}$ where A or B denotes one element type. Fig. 7(b) shows the boundary conditions. As powder elements are not defined here, heat loss to the powder is modeled through boundary conditions by identifying a convection coefficient to the part side surface ($h_{part,side}$), the support side surface ($h_{supp,side}$), the top surface (h_{top}), and substrate surfaces (h_{subs}). Note that a single convective coefficient is assumed for all substrate surfaces for simplicity.

Case II: With powder elements. As illustrated in Fig. 5, powder is shown as white space that fills in multiple regions including inside the inner wall, between the inner wall and support structure, between the support structure and the outer wall, and outside the outer wall. Rather than defining a powder element for each of these regions in each grouped layer, for simplicity, a single synthetic, aggregate powder element is defined for each grouped layer, connected to all other elements in that layer as illustrated in Fig. 8. The edge between the powder element and each part or support element denotes that the part or support component has surface contact with powder. This aggregate powder element can be viewed as replacing the "air" next to the part or support in Fig. 7(b) so that the surface convection of part- or support-side in Case I can be replaced by heat transfer from the part- or support-side to the powder element. Temperature of the aggregate powder element is an indication for the average temperature of all powder in this grouped layer.

Consider that layer ℓ is under melting. The energy balance in Eq. (18) is modified to include the powder elements:

$$\underbrace{\frac{A_{cs}^i \rho_i c_{p,i} \Delta x_i}{\Delta t}(T_i^{p+1} - T_i^p)}_{\text{Rate of energy change}} = \underbrace{\sum_{j \in \mathcal{N}_i^\ell} \frac{A_{ol}^{i,j} \kappa_{i,j}}{\delta_{i,j}}(T_j^{p+1} - T_i^{p+1})}_{\text{Conduction}} + \underbrace{A_{sf}^i h_i (T_a - T_i^{p+1})}_{\text{Convection on surfaces to the surroundings}} + \underbrace{\sum_{k \in \mathcal{E}_i^\ell} A_{powd}^{i,k} \gamma_{i,k}(T_k^{p+1} - T_i^{p+1})}_{\text{Heat loss from fused solid components to powder elements}} \tag{19}$$

- When element i represents a powder element, the first RHS term computes the thermal conduction among i and its neighboring powder elements in the neighboring layers. When i is a non-powder element, see the corresponding explanation in Case I.
- The second RHS term computes the convective heat loss to the surroundings (boundary conditions).
- The third RHS term computes the heat losses from fused solid component (which can be part, support, or substrate) to the powder elements, where $\gamma_{i,k}$ denotes the heat transfer coefficient at the solid-powder interface (Fig. 7(a)) with $A_{powd}^{i,k}$ denoting the interface area. When element i represents a solid component, $\mathcal{E}_i^\ell$ represents the set of neighboring powder elements; when element i represents a powder element, $\mathcal{E}_i^\ell$ represents the set of neighboring solid elements.

Fig. 7(c) shows the updated boundary conditions after including the powder elements. The heat losses to the surroundings are considered at the top surface (h_{top}), the powder bed side surface ($h_{powd,side}$), and the substrate surfaces (h_{subs}).

Note that although the derivation of Eqs. (18) and (19) here is illustrated through a case study for the square-canonical geometry,

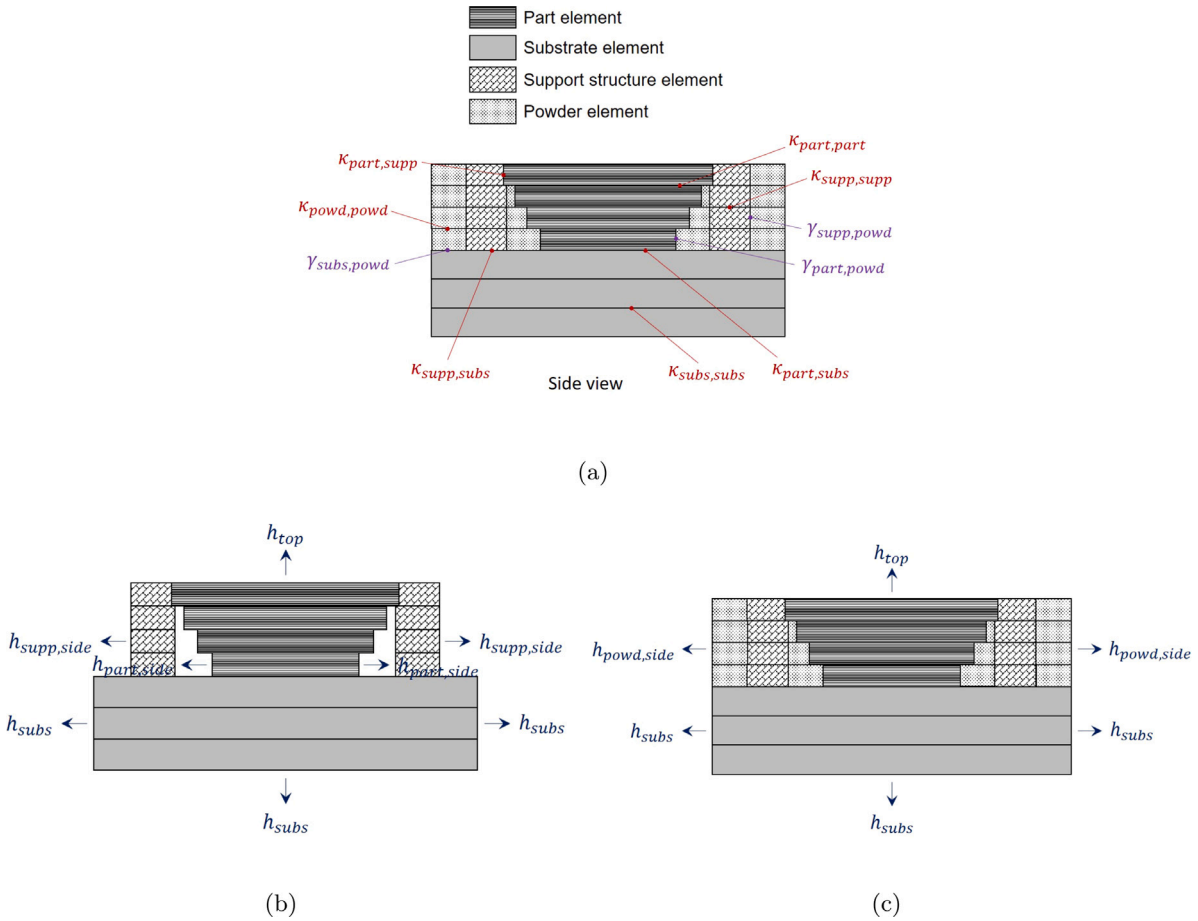

Fig. 7. (a) Illustration of four types of elements and heat transfer among them; for clarity, only part elements for inner-wall are included in the side-view plot. (b) Boundary conditions for model without powder elements; (c) Boundary conditions for model with powder elements.

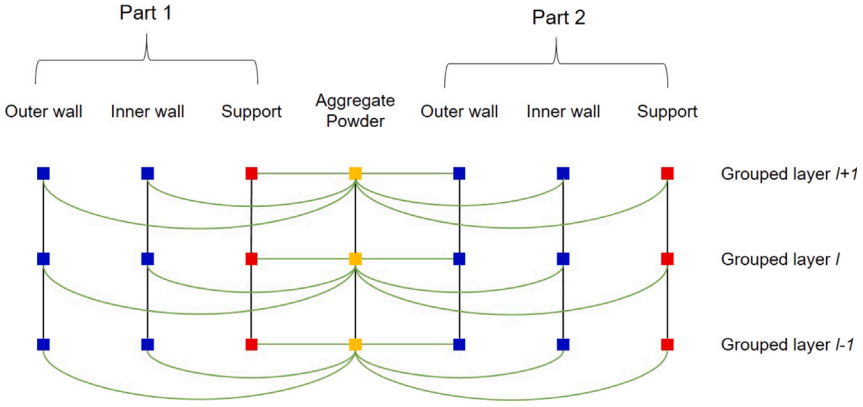

Fig. 8. Schematic illustration of how the aggregate powder element in each grouped layer is connected to other elements.

equations in this part-scale thermal model are applicable to a general AM part, as they have accounted for all four general elements of an AM process including the part, substrate, support, and powder elements.

4.2.2. Finite difference model in a matrix format

Similar to the 1D problem, the FDM part-scale thermal model for a 3D part can be put into a matrix format. Consider layer ℓ and time increment p, and define the vector $\mathbf{T}_\ell^p = [T_1^p, \ldots, T_{N_\ell}^p]^\top$, where N_ℓ denotes the total number of elements on and beneath layer ℓ (see Fig. 8). Further define

$$a_i = \frac{A_{cs}^i \rho_i c_{p,i} \Delta x_i}{\Delta t}, \quad b_{i,j} = \frac{A_{ol}^{i,j} \kappa_{i,j}}{\delta_{i,j}}, \quad c_{i,k} = A_{powd}^{i,k} \gamma_{i,k}, \quad r_i = A_{air}^i h_i \tag{20}$$

Then, Eq. (19) can be rewritten in the following compact form

$$\mathbf{\Gamma} \mathbf{T}_\ell^{p+1} = \mathbf{\Lambda} \mathbf{T}_\ell^p + \mathbf{R} T_a \tag{21}$$

$$\begin{bmatrix} a_1 + \sum_{j\in\mathcal{N}_1^\ell} b_{1,j} + \sum_{k\in\mathcal{E}_1^\ell} c_{1,k} + r_1 & -b_{1,2} - c_{1,2} & \cdots & -b_{1,N_\ell} - c_{1,N_\ell} \\ -b_{2,1} - c_{2,1} & a_2 + \sum_{j\in\mathcal{N}_2^\ell} b_{2,j} + \sum_{k\in\mathcal{E}_2^\ell} c_{2,k} + r_2 & \cdots & -b_{2,N_\ell} - c_{2,N_\ell} \\ \vdots & \vdots & \ddots & \vdots \\ -b_{N_\ell,1} - c_{N_\ell,1} & -b_{N_\ell,2} - c_{N_\ell,2} & \cdots & a_{N_\ell} + \sum_{j\in\mathcal{N}_{N_\ell}^\ell} b_{N_\ell,j} + \sum_{k\in\mathcal{E}_{N_\ell}^\ell} c_{N_\ell,k} + r_{N_\ell} \end{bmatrix} \tag{22}$$

Box I.

Table 3
Constant material properties for Inconel 718 and tool steel used in the models.

Parameter	Value	Unit
Density (Inconel 718)	8.146×10^{-6}	kg/mm^3
Density (Tool steel)	8.0×10^{-6}	kg/mm^3
Conductivity (Inconel 718)	0.0114	W/mm K
Conductivity (Tool steel)	0.0243	W/mm K
Specific heat (Inconel 718)	427	J/kg K
Specific heat (Tool steel)	460	J/kg K

where $\mathbf{\Gamma} =$ (see Box I)

$$\mathbf{\Lambda} = \text{diag}(a_1, \ldots, a_{N_\ell}), \tag{23}$$

$$\mathbf{R} = [r_1, r_2, \ldots, r_{N_\ell}]^\top. \tag{24}$$

In terms of the network structure shown in Figs. 6 and 8, many terms of $b_{i,j}$ and $c_{i,j}$ are zero and hence, the matrix $\mathbf{\Gamma}$ is sparse.

The total simulation period for building layer ℓ is computed as $t_{tot}^\ell = t_{proc}^\ell + t_{recoat}^\ell$, where t_{proc}^ℓ and t_{recoat}^ℓ denote the respective laser processing time and recoating time for layer ℓ. Then during t_{tot}^ℓ, an update rule for the part-level temperature field can be derived from Eq. (21) as

$$\mathbf{T}_\ell^{p+1} = \mathbf{\Gamma}^{-1}(\mathbf{\Lambda}\mathbf{T}_\ell^p + \mathbf{R}T_a), \quad p = 0, \ldots, n_\ell - 1 \tag{25}$$

where n_ℓ is the maximum time index for t_{tot}^ℓ.

The next is to determine the initial condition $\mathbf{T}_\ell^0$ in Eq. (25). Recall that N_ℓ denotes the total number of elements on and beneath layer ℓ. Let m_ℓ denote the number of elements on layer ℓ, and let $\mathbf{T}_{act}^\ell$ denote the vector of activation temperature for these m_ℓ number of elements. The initial condition $\mathbf{T}_\ell^0$ can be constructed from $\mathbf{T}_{\ell-1}^{n_{(\ell-1)}}$, which is the temperature vector at the final time index $n_{(\ell-1)}$ of the previous layer $(\ell - 1)$, and the activation temperature for layer ℓ as follows:

$$\mathbf{T}_\ell^0 = \left[(\mathbf{T}_{\ell-1}^{n_{(\ell-1)}})^\top \quad (\mathbf{T}_{act}^\ell)^\top\right]^\top \tag{26}$$

As shown in Table 2, the laser power values for melting the part and support structures are different for the square-canonical geometry, which justifies different activation temperatures for the part and support elements. For powder elements in the model, as they are not melted by the laser, the activation temperature is set to be the ambient temperature T_a if the powder is not preheated.

The resulting interlayer temperature $\mathbf{T}_\ell^{inter}$ (a vector with a dimension of $m_\ell \times 1$) for the m_ℓ number of elements on layer ℓ can be obtained by extracting the last m_ℓ elements from $\mathbf{T}_\ell^{n_\ell}$ as follows:

$$\mathbf{T}_\ell^{inter} = \mathbf{S}\mathbf{T}_\ell^{n_\ell} \tag{27}$$

where $\mathbf{S}$ is a $m_\ell \times N_\ell$ matrix with its elements $s(i, j) = 1$ when $i \le m_\ell$ and $i + j = N_\ell + 1$; otherwise $s(i, j) = 0$.

4.2.3. Material properties

The FDM in this study assumes constant material properties. Table 3 lists the constant material parameters for Inconel 718 (used for the part and support) and tool steel (used for the substrate). In Eqs. (18) and (19), when the node i and node j are of the same solid material, the thermal conductivity $\kappa_{i,j} = \kappa_i$. This applies to the conductivity among adjacent nodes of the same element type. When the two nodes are of different material, an equivalent thermal conductivity $\kappa_{i,j}$ can be computed by [53]:

$$\frac{1}{\kappa_{i,j}} = \frac{1}{\kappa_i} + \frac{1}{\kappa_j} \tag{28}$$

This is used to compute the equivalent thermal conductivity $\kappa_{part,subs}$. For a porous support structure with a volume fraction ν, by omitting the effects of pore orientation and position on thermal conductance, the effective material density and thermal conductivity of the porous support structure can be computed by [54,55]:

$$\rho_{supp} = \nu \cdot \rho_s, \quad \kappa_{supp} = \nu \cdot \kappa_s \tag{29}$$

where ρ_s and κ_s are density and thermal conductivity of the corresponding solid material. This equation is used to compute the effective thermal conductivity of the porous support structure $\kappa_{supp,supp}$. After κ_{supp} is computed, Eq. (28) is then applied to compute $\kappa_{part,supp}$, and $\kappa_{subs,supp}$.

When powder elements are considered in the modeling, the powder-bed density of an powder element is assumed to be 60% of the density of the solid material [56]. Thermal conductivity of powder depends on many factors such as the relative density of the packed powder material, powder particle size distribution, pressure and temperature [56–58].

4.3. Experimental data

Without loss of generality, the measured interlayer temperature of the left canonical geometry is used here to evaluate the FDM computation. The interlayer temperature at each grouped layer ℓ corresponds to the interlayer temperature at physical layer of $18 \cdot \ell$. The mean and standard deviation of the interlayer temperature within each disjointed component of the layer (e.g., the inner- and outer-wall interlayer temperature respectively) are first extracted according to the slicing of the part geometry. Fig. 9(a) shows the interlayer temperature at a representative grouped layer $\ell = 40$. Fig. 9(b) illustrates how the STL of the build is used to identify a region of interest so that the mean and variance of each region's interlayer temperature can be computed.

Fig. 10 plots the mean and variance of the inner- and outer-wall interlayer temperature with respect to the grouped layer number, extracted from the measured temperature distributions. The interlayer temperature evolution is highly correlated with the part geometry and support structures used in the build process. The temperature difference between the inner- and outer-wall is small before the grouped layer No. 30, but afterwards, the temperature of the inner wall increases much faster than the outer-wall, leading to an increasing gap between the two branches representing the inner- and outer-wall temperature. Such

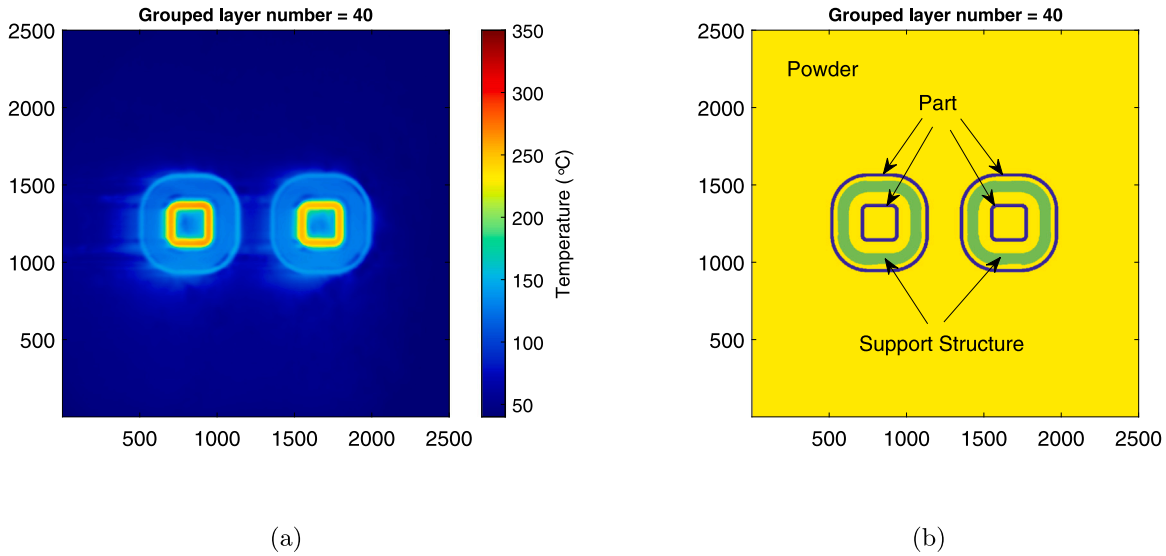

Fig. 9. (a) Measured interlayer temperature distribution at the grouped layer ℓ = 40 (physical layer No. 720); (b) Masks derived from STL to identify the regions of interest for computing mean/variance of interlayer temperature of each part component.

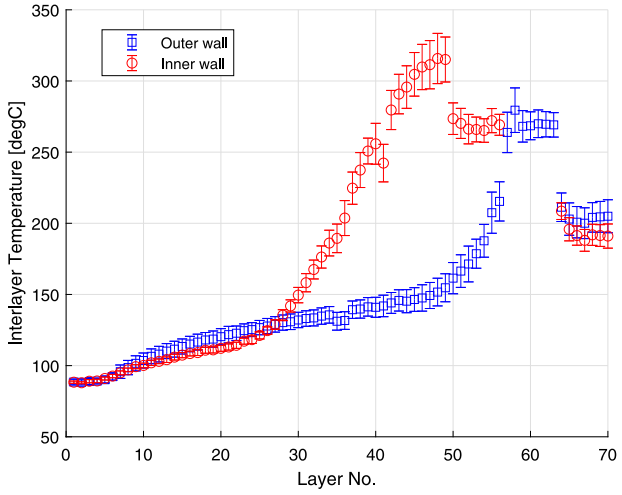

Fig. 10. Measured interlayer temperature (mean and std) of the inner- and outer-wall of the left canonical part.

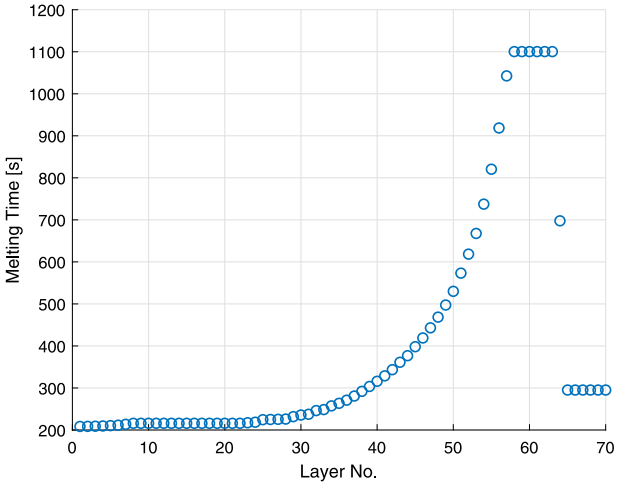

Fig. 11. Processing time for each grouped layer.

rapid increase in inner-wall temperature is due to the mass growth of the inner wall but there is not sufficient path for the accumulated heat to conduct into the substrate. The inner-wall temperature had a sudden drop at around the grouped layer No. 50, where the main support structure comes in contact with the inner wall surface and serves as an additional path of heat transfer to the substrate. Meanwhile, the thickness of the outer-wall starts to grow, causing a faster increasing of the outer-wall temperature. The inner- and outer-wall join together at around the grouped layer No. 57, where the outer-wall temperature is brought up and the two temperature branches merge. At about the grouped layer No. 64, the two walls split again, causing a temperature drop for both walls.

Note that the variance of the interlayer temperature for either the inner- or outer-wall is small, with the coefficient of variation (CV) (the ratio of the standard deviation to the mean) less than 0.073. During layer No. 42–50 when the inner-wall's cross-sectional area grows the most, the standard deviation of its interlayer temperature is less than 17.7 °C with COV less than 0.056. Note that when inner- and outer-walls merged into a single junction (grouped layer No. 57–63), the corresponding standard deviations of interlayer temperature appear to be lower than those in layer No. 42–50, indicating that the small variance in interlayer temperature is not necessarily limited to thin walls. The relative small CV in interlayer temperature justifies the modeling assumption that a single element is assigned to the inner- or outer-wall in each layer in this study. Furthermore, as discussed in Section 4.2.1, the standard deviation of mean interlayer temperature across the 18 physical layers of each grouped layer is less than 10 °C, which is smaller than the largest standard deviation of interlayer temperature distribution of 17.7 °C and thus supports the adoption of the layer scaling technique.

The laser processing time t^{ℓ}_{proc} for each grouped layer ℓ is plotted in Fig. 11. It accounts for scanning both the square-canonical parts and their associated support structures when applicable in each grouped layer. The recoating time $t^{\ell}_{recoate}$ equals to the number of physical layers in one grouped layer (18 physical layers here) multiplying the recoating time of each physical layer, which is machine specific and given in Table 2.

4.4. Identification of model parameters

In order to understand the respective contribution of including support elements and powder elements in the modeling, we evaluate

Table 4
Thermal parameters in the finite-difference models, where prefix * denotes that the parameter is identified using experimental measurements.

Category	Parameter	$\mathcal{M}_{(part/sub)}$	$\mathcal{M}_{(part/sub,supp)}$	$\mathcal{M}_{(part/sub,supp,powd)}$
Conduction (W/mm K)	$\kappa_{part,part}$	0.0114	0.0114	0.0114
	$\kappa_{subs,subs}$	0.0243	0.0243	0.0243
	$\kappa_{part,subs}$	0.0078	0.0078	0.0078
	$\kappa_{supp,supp}$	/	0.0031	0.0031
	$\kappa_{part,supp}$	/	0.0024	0.0024
	$\kappa_{subs,supp}$	/	0.0027	0.0027
	$^*\kappa_{powd,powd}$	/	/	1.0e−5
Convection boundary conditions (W/mm^2 K)	h_{top}	1.0e−5	1.0e−5	1.0e−5
	$^*h_{part,side}$	1.4e−5	1.4e−5	/
	$^*h_{subs}$	7.0e−6	7.0e−6	2.6e−5
	$h_{supp,side}$	/	3.78e−6	/
	$^*h_{powd,side}$	/	/	1.0e−6
Heat transfer between solid and powder elements (W/mm^2 K)	$^*\gamma_{part,powd}$	/	/	3.1e−5
	$^*\gamma_{subs,powd}$	/	/	3.3e−5
	$\gamma_{supp,powd}$	/	/	8.4e−6

the following three models with increasing complexity, where the first two are simplified ones of the full model in (Eq. (25)–Eq. (27)):

- $\mathcal{M}_{(part/sub)}$: Only part and substrate elements are included in the finite-difference model;
- $\mathcal{M}_{(part/sub,supp)}$: Support elements are added to the model $\mathcal{M}_{(part/sub)}$, see Eq. (18);
- $\mathcal{M}_{(part/sub,supp,powd)}$: Powder elements are added to $\mathcal{M}_{(part/sub,supp)}$, see Eq. (19) (or Eq. (25)–Eq. (27)).

Thermal parameters used in the three models are given in Table 4, which include two groups: (i) equivalent material properties computed from Table 3; and (ii) model parameters that are identified from matching the model-computed interlayer temperature with experimental data. The identified parameters are annotated with "*" in Table 4.

The heat convection coefficient on the top surface h_{top} is preset to $h_{top} = 10^{-5}$ W/mm^2 K for all three models in terms of the existing literature [26,47]. For $\mathcal{M}_{(part/sub)}$, the convection coefficients $h_{part,side}$ and h_{subs} are identified by minimizing the root-mean-squared error (RMSE) between the model's computed interlayer temperature and the mean of the measured interlayer temperature, where the entire experimental dataset for the 70 grouped layers is used. The resulting convection coefficient values are consistent with the reported ranges used in the existing finite-element models, e.g., convection coefficients of $5\times10^{-6}-30\times10^{-6}$ W/mm^2 K were used in [47] and $5\times10^{-6}-50\times10^{-6}$ W/mm^2 K were used in [26]. For $\mathcal{M}_{(part/sub,supp)}$, the heat convection coefficients $h_{part,side}$ and h_{subs} are not re-identified but following the same values from $\mathcal{M}_{(part/sub)}$; $h_{supp,side}$ is set as $h_{supp,side} = \nu \cdot h_{part,side}$ with the volume fraction $\nu = 0.27$.

For $\mathcal{M}_{(part/sub,supp,powd)}$, thermal properties related to the powder elements and heat convection coefficients at the boundary conditions are again identified to minimize the RMSE with respect to the mean of the measured interlayer temperature, but only randomly-selected half of the experimental data are used for model training. Note that h_{subs} in this model is re-identified as h_{subs} only needs to account for the side and bottom of the substrate in contrast to that h_{subs} in $\mathcal{M}_{(part/sub)}$ also accounts for convection at the top area of the substrate that is not occupied by the part. The resulting h_{subs} value still falls within the reported range of convection coefficients ($5\times10^{-6}-50\times10^{-6}$ W/mm^2 K) used in the part-scale, finite-element models [26,47]. The identified heat transfer coefficients between the solid and the powder (approximated as convection) also fall within the regular ranges of convection coefficients used in [26,47]. The parameter $\gamma_{supp,powd}$ is set as $\gamma_{part,powd}$ multiplying the volume fraction. The identified convection coefficient $h_{powd,side}$ is much lower than other convection coefficients, indicating that it is almost insulated between the powder and the wall of the machine chamber. The identified thermal conductivity of Inconel 718 powder, $\kappa_{powd,powd}$, is about 0.1% of its solid material, which is consistent with the reported value given in the study by Wei et al. [57], where the thermal conductivity of Inconel 718 powder bed sample was shown to be about 0.2% of its solid, bulk thermal conductivity. Overall, with the identified values of heat-transfer parameters falling within their respective range of commonly used values in the existing studies, they are expected to be transferable for modeling other geometries.

4.5. Results on model evaluation

After the model parameters are identified, the model-computed interlayer temperature is plotted in Fig. 12. Fig. 12(a) shows that the model $\mathcal{M}_{(part/sub)}$ is able to capture the trend of the inner-wall interlayer temperature reasonably well before the grouped layer No. 50. However, in contrast to that the measured temperature starts to drop at layer No. 50 (caused by support structure in contact with the inner wall), the computed inner-wall temperature keeps increasing during layer No. 50–56. In addition, $\mathcal{M}_{(part/sub)}$ computes that the temperature of the outer wall first increases, achieves its peak value around layer No. 30, and then decreases. This does not match with the steady increasing trend of the measured outer-wall interlayer temperature. Such discrepancy in both inner- and outer-wall temperature between $\mathcal{M}_{(part/sub)}$ and the measurements cannot be corrected by just tuning the convection coefficients in $\mathcal{M}_{(part/sub)}$, noting that all experimental data were used for model training.

Effect of including support elements. Fig. 12(b) shows that by adding the support elements into the modeling, $\mathcal{M}_{(part/sub,supp)}$ is able to capture the inner-wall's temperature drop in layer No. 50–56, although $\mathcal{M}_{(part/sub,supp)}$ has over-computed the inner-wall temperature right before layer No. 50. However, $\mathcal{M}_{(part/sub,supp)}$ has not changed the decreasing trend of the outer-wall temperature after layer No. 30. Such discrepancy in the outer-wall temperature has a trickle-down effect to later layers, causing large errors when the two walls start to merge around layer No. 57.

Effect of including powder elements. As discussed in Section 4.4, randomly-selected half of the experimental data are used for identifying the parameters of $\mathcal{M}_{(part/sub,supp,powd)}$ (model training), and then the other half of the experimental data are used for model testing. Fig. 12(c) shows the model computed interlayer temperature versus the training and testing samples. After including powder elements, the outer-wall temperature computed by the model $\mathcal{M}_{(part/sub,supp,powd)}$ shows a gradual increase after the grouped layer No. 30, i.e., following a similar trend as the measurement. On the other hand, by including powder elements, the inner-wall temperature after layer No. 30 is lower

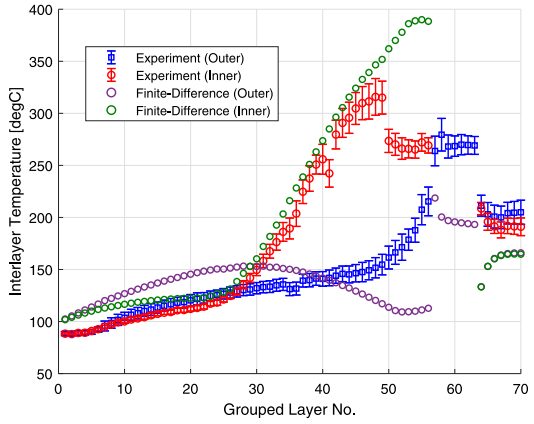

(a) $\mathcal{M}_{(part/sub)}$

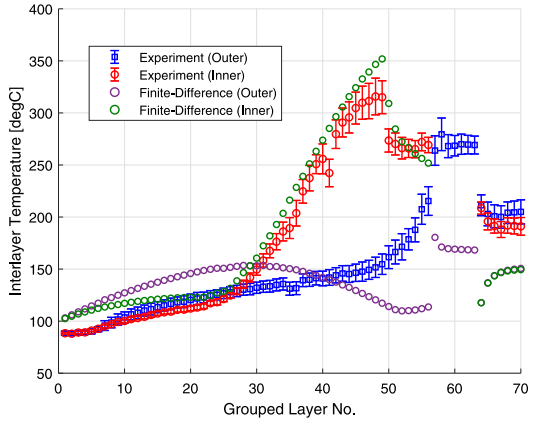

(b) $\mathcal{M}_{(part/sub,supp)}$

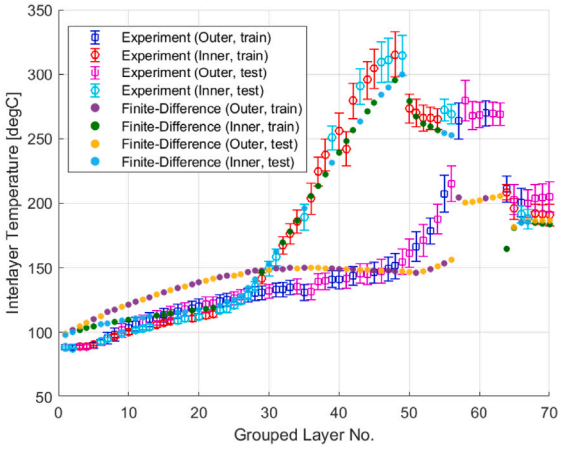

(c) $\mathcal{M}_{(part/sub,supp,powd)}$

Fig. 12. Finite-difference computation versus measurements of interlayer temperature.

than its counterpart computed by $\mathcal{M}_{(part/sub,supp)}$. Essentially, the newly added aggregate powder elements serve as a medium that brings the temperatures of the inner- and outer-wall closer, as the drastically accumulated heat in the inner-wall after layer No. 30 causes heat transfer to the powder and then to the outer wall, contributing to the outer-wall temperature increase after layer No. 30.

Nevertheless, the increasing slope of the outer-wall temperature computed by $\mathcal{M}_{(part/sub,supp,powd)}$ is smaller than the slope from the measurement, resulting in under-estimation of the outer-wall temperature before the outer wall starts to merge with the inner wall at layer No. 57. As a result, the model-computed junction temperature is lower than the measurements.

Overall, the model comparison demonstrates that including the support-structure elements and powder elements in the FDM is essential to capture the key characteristics of part-scale temperature evolution. Without including these elements, simply tuning model parameters such as convection coefficients is not able to capture critical trends in the interlayer temperature evolution. Table 5 provides a summary of the RMSE values between each model's computed interlayer temperature and the mean of the measured temperature. With the increase of the model complexity, the RMSE is reduced as expected, with the RMSE of the full model ranging from 20 °C–25 °C with respect to training and testing samples respectively. Noting that the largest standard deviation of an interlayer temperature distribution is about 18 °C (Section 4.3), such modeling error is comparable to the standard deviation of the interlayer temperature distribution and thus is considered acceptable for part-scale thermal control.

Table 5
Root-mean-square error (RMSE) between the model computation and mean of the measured interlayer temperature.

Model	RMSE (°C)	
$\mathcal{M}_{(part/sub)}$	41.47	
$\mathcal{M}_{(part/sub,supp)}$	38.61	
	training	testing
$\mathcal{M}_{(part/sub,supp,powd)}$	20.22	24.64

5. Model based part-level thermal control

Recall that interlayer temperature acts as the initial background temperature under which each new layer is scanned. As discussed in the introduction, several studies [43–45] investigated how the initial temperature could affect the melt-pool morphology and build quality. Hence, it would be useful to investigate layer-by-layer optimization of process parameters, e.g., laser power, to enforce that the interlayer temperature stays within a relative low range to reduce the risk of overheating. The FDM part-scale thermal model derived in early sections can be used to enable the optimization of process parameters at each grouped layer.

Control variables. For each grouped layer, consider that laser power is the only control variable, with all other process parameters fixed. Let $\mathbf{P}_\ell$ denote the vector of laser power for the grouped layer ℓ, with each vector element $P_\ell^{(i)}$ corresponding to laser power applied to each part or support element in the layer. Thus, $\mathbf{P}_\ell$ is the control vector in the optimization problem.

Optimal control problem. For each grouped layer ℓ, a generic optimal control problem can be formulated as follows:

$$\min_{\mathbf{P}_\ell} \; J(\mathbf{T}_\ell^{inter}, \overline{\mathbf{T}}_\ell^{inter}, \mathbf{P}_\ell) \tag{30}$$

$$\begin{aligned} s.t.\;\; & \mathbf{T}_\ell^{p+1} = \mathbf{\Gamma}^{-1}(\mathbf{\Lambda}\mathbf{T}_\ell^{p} + \mathbf{R}T_a), \quad p = 0, \dots, n_\ell - 1 \\ & \mathbf{T}_\ell^{0} = \left[(\mathbf{T}_{\ell-1}^{n_{(\ell-1)}})^\top \quad (\mathbf{T}_{act}(\mathbf{P}_\ell))^\top\right]^\top \\ & \mathbf{T}_\ell^{inter} = \mathbf{S}\mathbf{T}_\ell^{n_\ell} \\ & \mathbf{P}_\ell \in \mathbb{P} \end{aligned}$$

where Eq. (30) represents a generic cost function in terms of a prespecified target interlayer temperature $\overline{\mathbf{T}}_\ell^{inter}$. The three equations following (30) are from Eq. (25)–Eq. (27), representing the FDM thermal

model. The last constraint specifies that the laser power should be constrained within a feasible set $\mathbb{P}$.

Alternatively, constraints can be defined to enforce that the interlayer temperature does not exceed a certain threshold value to reduce the risk of overheating. For example, the cost function in Eq. (30) can be replaced by the following cost function on the laser power with an additional constraint on the interlayer temperature:

$$\min_{\mathbf{P}_\ell} \; J = \|\mathbf{P}_\ell - \mathbf{P}_{default}\|^2 \tag{31}$$

$$s.t. \;\; \mathbf{T}_\ell^{inter} \le \overline{\mathbf{T}}_\ell^{inter} \tag{32}$$

subject to the same thermal model; $\mathbf{P}_{default}$ denotes the vector of machine's default laser power values, which are often set through experimental trial-and-error by the machine manufacturers. Such a combination of cost function and constraint is defined to search for laser power values that are closest to machine's default values but able to enforce the interlayer temperature within a certain range. The optimization problem defined in Eqs. (31)–(32) under the thermal model (Eq. (25)–Eq. (27)) is a convex optimization problem.

Consider the square-canonical geometry as a demonstrating example for the constrained optimization (31)–(32). For simplicity of illustration, further consider the laser power scanning the part as the only control variable, with the laser power scanning the support structure fixed to its default value as in Table 2. Fig. 13 shows results to the convex optimization, where the default power for melting the build part is set to 285 W as in Table 2 and the reference interlayer temperature is set to be 200 °C. Fig. 13(a) shows that the interlayer temperature of the inner-wall or outer-wall is maintained under the reference value of 200 °C during the entire simulated build process. Fig. 13(b) plots the resulting optimal laser power profiles for the inner and outer walls, which are presented in the same figure as the FDM predicted interlayer temperature under the default laser power of 285 W. The interlayer temperature under the default laser power helps provide physical insights to interpret the optimal control trajectories. For example, for the first 35 layers where the interlayer temperatures of both inner- and outer-walls are below the reference value of 200 °C, the default laser power of 285 W is applied for both walls. After layer No. 35, the inner-wall temperature exceeds the reference value, which drives the laser power for the inner-wall to decrease as low as around 150 W. Future experimental work will need to investigate if this is a feasible laser power to melt metal powder. After layer No. 50, the inner-wall temperature is reduced, which pumps the laser power to increase but still lower than its default value of 285 W. As the outer-wall temperature remains lower than 200 °C before merging with the inner wall, the laser power for the outer wall remains close to 285 W. After layer No. 60, laser power has to be reduced from its default value to enforce the resulting interlayer temperature not exceeding the reference value of 200 °C. When the two walls separate again, the default laser power of 285 W is sufficient to keep the interlayer temperature under 200 °C and thus it is used for both walls.

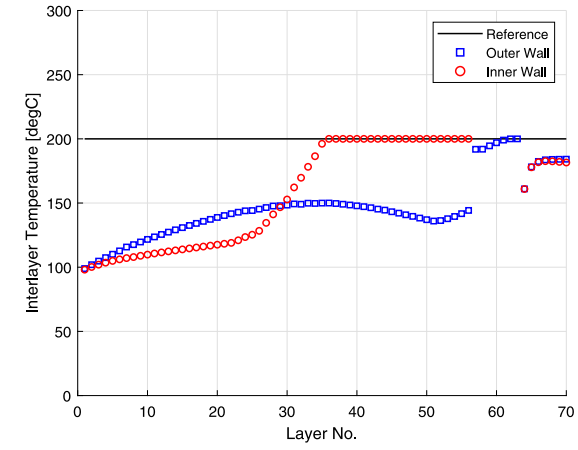

(a)

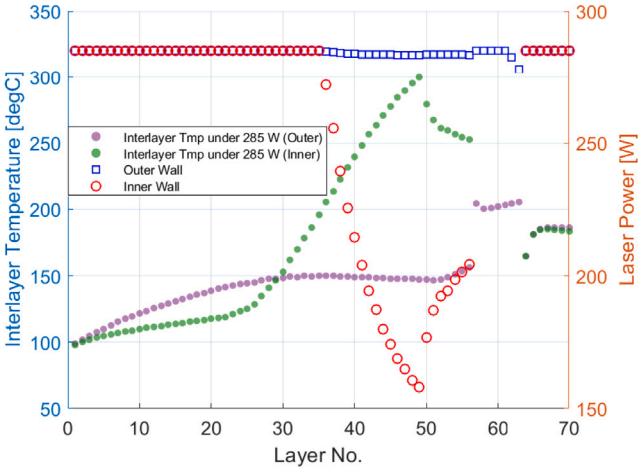

(b)

Fig. 13. Optimal control of laser power in each grouped layer for the square-canonical geometry. (a) Interlayer temperature constraint is enforced by the optimal control; (b) Inner- and outer-wall laser power profiles (right vertical axis) co-plotted with FDM predicted interlayer temperature (left vertical axis) under the default 285 W.

6. Runtime and its implication towards real-time implementation

The finite-difference models were coded in MATLAB and simulated on a Dell laptop with Intel®Core i7-3632QM CPU, 2.20 GHz. It took the models $\mathcal{M}_{(part/sub)}$ and $\mathcal{M}_{(part/sub,supp)}$ approximately 0.3 s and the model $\mathcal{M}_{(part/sub,supp,powd)}$ 0.8 s to simulate the temperature history and compute the interlayer temperature of the twin square-canonical parts. Sparsity of the matrix $\mathbf{\Gamma}$ in Eq. (25) was not explored here. The model-based part-level thermal control was coded in MATLAB using *cvx* package for convex optimization, and it took about 35 s to solve the optimal power profiles for the entire build as shown in Fig. 13. Note that most of the computation complexity of the FDM comes from matrix inversion for $\mathbf{\Gamma}$ in Eq. (25), for which the computation complexity is $\mathcal{O}((N_\ell)^3)$ if no sparsity of $\mathbf{\Gamma}$ is explored, where N_ℓ denotes the total number of elements on and beneath the layer ℓ. If no layer scaling is applied, the complexity of matrix inversion running on the physical layers is $\mathcal{O}(18^3)$ higher than using layer grouping of 18 physical layers. As a result, the runtime of model prediction plus optimization performed directly on physical layers is expected to be at the order of hours. Having said that, the current implementation using MATLAB and a dense equation solver is not optimal for memory utilization and speed. The nodal network of the proposed FDM results into a sparse matrix, which will scale much better in larger systems. However, this is outside of the scope of this paper.

Experimental validation of the part-scale thermal control in Section 5 will be conducted in the future work. There are two potential approaches to implement the proposed part-scale thermal control:

1. In a feedforward way, where offline-derived laser power profiles in Fig. 13 can be loaded to the EOS machine as a feedforward control to replace the default laser power values in the build process. This feedforward control itself does not require any in-situ sensing and data processing, and it has no requirement on the speed of model prediction or process optimization as they only need to be completed offline before the experiment. The downside of the feedforward control is that its control

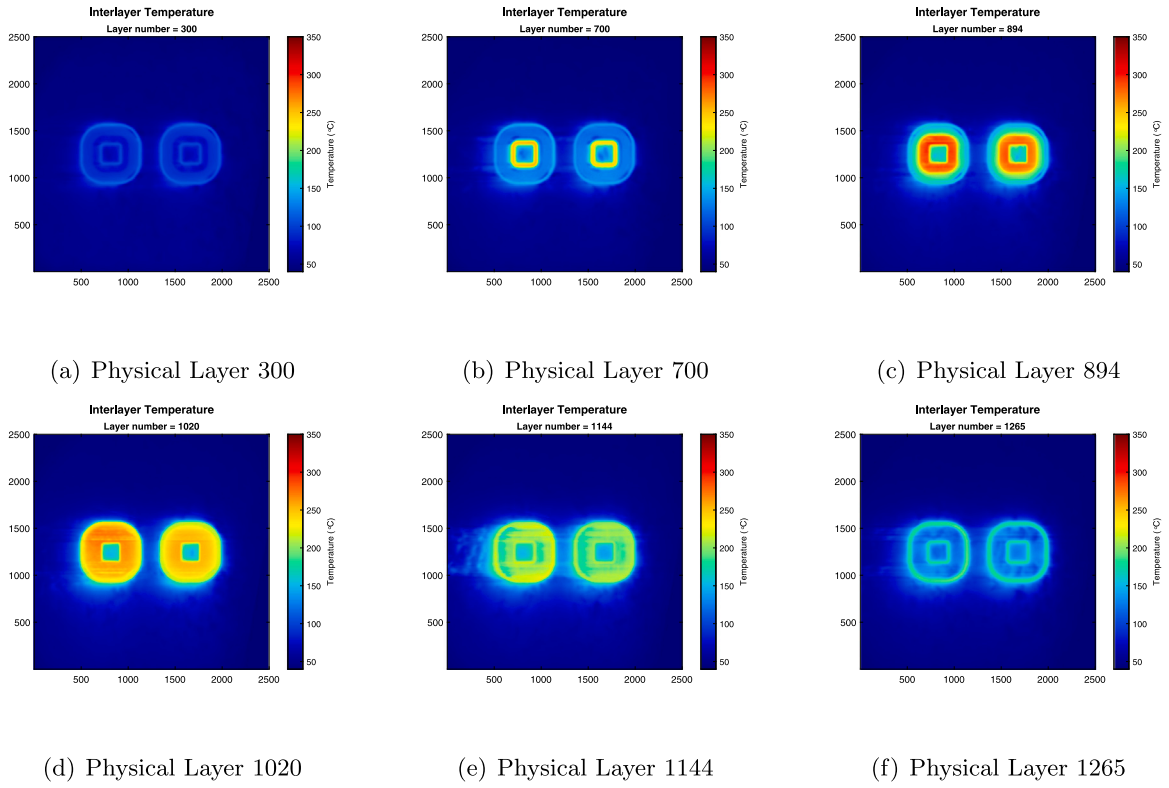

(a) Physical Layer 300 (b) Physical Layer 700 (c) Physical Layer 894

(d) Physical Layer 1020 (e) Physical Layer 1144 (f) Physical Layer 1265

Fig. 14. Interlayer temperature distribution at selected physical layers [51].

performance is subject to modeling errors and any unpredicted process disturbances that could occur during the build process.

2. Towards real-time implementation by utilizing the in-situ monitoring of interlayer temperature. In this approach, the first component of the initial condition $\mathbf{T}^0_\ell$ in Eq. (26) can be obtained from in-situ measurement rather than using model prediction from the previous layer $(\ell - 1)$, and thus it can avoid accumulating modeling errors across grouped layers. However, this approach puts a time limitation on how fast the model prediction and the resulting process optimization have to be performed. Applying the laser scaling scheme enables completing the model prediction and optimization within 2 s for each grouped layer, which opens up the opportunity for potential real-time implementation of the part-level thermal control during the interlayer dwell time. Adding a few extra seconds before scanning each grouped layer to prepare for the process-parameter optimization could potentially be an acceptable solution with minimal interruption to the normal build process.

7. Conclusion

This paper presented an FDM for fast computation of part-scale temperature evolution in L-PBF build process. By defining an element for each disjointed part component in each (grouped) layer, the proposed FDM modeled the part fabrication as a multi-branch network. Modeling results from this study showed that support elements and powder elements were essential in capturing the heat transfer in the L-PBF process. For a square-canonical geometry of Inconel 718 which was used as a case study for modeling of a 3D part, several heat-transfer model parameters were identified by matching the model computation with the in-situ measurements of interlayer temperature. The identified heat-transfer parameter values fall within their respective range of commonly used values in the existing finite-element models. The resulting model computed interlayer temperature has a root-mean-square error less than 25 °C with respect to the measurements including both training and testing samples. It was also demonstrated that the proposed FDM can be used for the design of part-scale thermal control. For the same square-canonical geometry, a preliminary numerical study showed that the layer-by-layer laser power profiles can be derived to enforce the interlayer temperature not exceeding a certain threshold value by solving a convex optimization problem. Future work will investigate different optimization formulations for part-scale thermal control using the proposed FDM, and conduct experimental evaluation on how different optimization formulations would affect the resulting microstructure and build quality.

Declaration of competing interest

The authors declare that they have no known competing financial interests or personal relationships that could have appeared to influence the work reported in this paper.

Acknowledgments

This work was supported in part by the U.S. National Science Foundation under Grant No. 2015930.

Appendix A. Fourier coefficients in the analytic solution to 1D problem

The initial conditions in Eqs. (8) and (11) are piecewise continuous. Even extension of the initial conditions in $[-L_j, L_j]$ is first constructed, and then the Fourier series expansion is performed as follows:

$$T^{(j)}(x,0) = \frac{c_0^{(j)}}{2} + \sum_{k=1}^{\infty} c_k^{(j)} \cos\left(\frac{k\pi x}{L_j}\right). \tag{33}$$

The coefficients $c_0^{(j)}$ and $c_k^{(j)}$ are computed by integration over the section $[-L_j, L_j]$ iteratively in the layer-by-layer manner. For the first

layer ($j = 1$),

$$c_0^{(1)} = \frac{1}{L_1}\int_{-L_1}^{L_1} T^{(1)}(x,0)dx = \frac{2(T_{act}l_t + T_a L_0)}{L_1} \tag{34}$$

$$c_k^{(1)} = \frac{1}{L_1}\int_{-L_1}^{L_1} T^{(1)}(x,0)\cos(\frac{k\pi x}{L_1})dx = \frac{2}{k\pi}(T_a - T_{act})\sin(\frac{k\pi L_0}{L_1}), \tag{35}$$

and then for the subsequent layers ($j = 2, 3, \dots$)

$$c_0^{(j)} = \frac{1}{L_j}\int_{-L_j}^{L_j} T^{(j)}(x,0)dx = \frac{2T_{act}l_t}{L_j} + \frac{L_{j-1}}{L_j}c_0^{(j-1)} \tag{36}$$

$$\begin{aligned} c_k^{(j)} &= \frac{1}{L_j}\int_{-L_j}^{L_j} T^{(j)}(x,0)\cos(\frac{k\pi x}{L_j})dx \\ &= \frac{c_0^{(j-1)} - 2T_{act}}{k\pi}\sin(\frac{k\pi L_{j-1}}{L_j}) \\ &+ \sum_{m=1}^{\infty} c_m^{(j-1)} e^{-\alpha\left(\frac{m\pi}{L_{j-1}}\right)^2 t_{tot}} \left[\frac{L_{j-1}}{(mL_j - kL_{j-1})\pi}\sin(m\pi - \frac{k\pi L_{j-1}}{L_j}) \right. \\ &\left. + \frac{L_{j-1}}{(mL_j + kL_{j-1})\pi}\sin(m\pi + \frac{k\pi L_{j-1}}{L_j}) \right]. \end{aligned} \tag{37}$$

Once the coefficients $c_0^{(j)}$ and $c_k^{(j)}$ are determined, the analytical solution in the form of Eq. (12) can be obtained explicitly.

Appendix B. In-situ measurements of interlayer temperature

Fig. 14 shows the interlayer temperature distribution at several representative physical layers, where a lookup table built from calibration data is used to convert the IR radiance to temperature. Readers are referred to [51] for details of the calibration and lookup table.

References

[1] Levy GN, Schindel R, Kruth J-P. Rapid manufacturing and rapid tooling with layer manufacturing (LM) technologies, state of the art and future perspectives. CIRP Ann 2003;52(2):589–609.

[2] Kruth J-P, Levy G, Klocke F, Childs T. Consolidation phenomena in laser and powder-bed based layered manufacturing. CIRP Ann 2007;56(2):730–59.

[3] Markl M, Körner C. Multiscale modeling of powder bed–based additive manufacturing. Annu Rev Mater Res 2016;46:93–123.

[4] King WE, Anderson AT, Ferencz R, Hodge N, Kamath C, Khairallah SA, et al. Laser powder bed fusion additive manufacturing of metals; physics, computational, and materials challenges. Appl Phys Rev 2015;2(4):041304.

[5] Körner C, Attar E, Heinl P. Mesoscopic simulation of selective beam melting processes. J Mater Process Technol 2011;211(6):978–87.

[6] Ammer R, Markl M, Ljungblad U, Körner C, Rüde U. Simulating fast electron beam melting with a parallel thermal free surface lattice Boltzmann method. Comput Math Appl 2014;67(2):318–30.

[7] Qiu C, Panwisawas C, Ward M, Basoalto HC, Brooks JW, Attallah MM. On the role of melt flow into the surface structure and porosity development during selective laser melting. Acta Mater 2015;96:72–9.

[8] King W, Anderson AT, Ferencz RM, Hodge NE, Kamath C, Khairallah SA. Overview of modelling and simulation of metal powder bed fusion process at Lawrence Livermore National Laboratory. Mater Sci Technol 2015;31(8):957–68.

[9] Lee Y, Zhang W. Modeling of heat transfer, fluid flow and solidification microstructure of nickel-base superalloy fabricated by laser powder bed fusion. Addit Manuf 2016;12:178–88.

[10] Khairallah SA, Anderson AT, Rubenchik A, King WE. Laser powder-bed fusion additive manufacturing: Physics of complex melt flow and formation mechanisms of pores, spatter, and denudation zones. Acta Mater 2016;108:36–45.

[11] Yan W, Qian Y, Ge W, Lin S, Liu WK, Lin F, et al. Meso-scale modeling of multiple-layer fabrication process in selective electron beam melting: inter-layer/track voids formation. Mater Des 2018;141:210–9.

[12] Fotovvati B, Chou K. Multi-layer thermo-fluid modeling of powder bed fusion (PBF) process. J Manuf Process 2022;83:203–11.

[13] Gusarov A, Yadroitsev I, Bertrand P, Smurov I. Heat transfer modelling and stability analysis of selective laser melting. Appl Surf Sci 2007;254(4):975–9.

[14] Dai D, Gu D. Tailoring surface quality through mass and momentum transfer modeling using a volume of fluid method in selective laser melting of TiC/AlSi10Mg powder. Int J Mach Tools Manuf 2015;88:95–107.

[15] Childs T, Hauser C, Badrossamay M. Mapping and modelling single scan track formation in direct metal selective laser melting. CIRP Ann 2004;53(1):191–4.

[16] Tseng W, Aoh J. Simulation study on laser cladding on preplaced powder layer with a tailored laser heat source. Opt Laser Technol 2013;48:141–52.

[17] Loh L-E, Chua C-K, Yeong W-Y, Song J, Mapar M, Sing S-L, et al. Numerical investigation and an effective modelling on the Selective Laser Melting (SLM) process with aluminium alloy 6061. Int J Heat Mass Transfer 2015;80:288–300.

[18] Dortkasli K, Isik M, Demir E. A thermal finite element model with efficient computation of surface heat fluxes for directed-energy deposition process and application to laser metal deposition of IN718. J Manuf Process 2022;79:369–82.

[19] Nandi SK, Kumar R, Agrawal A. Computationally inexpensive semi-analytical thermal model to predict melt-pool dimensions for a single-track in Selective Laser Melting. J Manuf Process 2022;80:469–79.

[20] Patil RB, Yadava V. Finite element analysis of temperature distribution in single metallic powder layer during metal laser sintering. Int J Mach Tools Manuf 2007;47(7–8):1069–80.

[21] Hussein A, Hao L, Yan C, Everson R. Finite element simulation of the temperature and stress fields in single layers built without-support in selective laser melting. Mater Des (1980-2015) 2013;52:638–47.

[22] Cheng B, Shrestha S, Chou K. Stress and deformation evaluations of scanning strategy effect in selective laser melting. Addit Manuf 2016;12:240–51.

[23] Foroozmehr A, Badrossamay M, Foroozmehr E, Golabi S. Finite element simulation of selective laser melting process considering optical penetration depth of laser in powder bed. Mater Des 2016;89:255–63.

[24] Gouge M, Michaleris P. Thermo-mechanical modeling of additive manufacturing. Butterworth-Heinemann; 2017.

[25] Matsumoto M, Shiomi M, Osakada K, Abe F. Finite element analysis of single layer forming on metallic powder bed in rapid prototyping by selective laser processing. Int J Mach Tools Manuf 2002;42(1):61–7.

[26] Dugast F, Apostolou P, Fernandez A, Dong W, Chen Q, Strayer S, et al. Part-scale thermal process modeling for laser powder bed fusion with matrix-free method and GPU computing. Addit Manuf 2021;37:101732.

[27] Denlinger ER, Gouge M, Irwin J, Michaleris P. Thermomechanical model development and in situ experimental validation of the Laser Powder-Bed Fusion process. Addit Manuf 2017;16:73–80.

[28] Kolossov S, Boillat E, Glardon R, Fischer P, Locher M. 3D FE simulation for temperature evolution in the selective laser sintering process. Int J Mach Tools Manuf 2004;44(2–3):117–23.

[29] Yin J, Zhu H, Ke L, Lei W, Dai C, Zuo D. Simulation of temperature distribution in single metallic powder layer for laser micro-sintering. Comput Mater Sci 2012;53(1):333–9.

[30] Roberts I, Wang C, Esterlein R, Stanford M, Mynors D. A three-dimensional finite element analysis of the temperature field during laser melting of metal powders in additive layer manufacturing. Int J Mach Tools Manuf 2009;49(12):916–23.

[31] Contuzzi N, Campanelli S, Ludovico A. 3 d finite element analysis in the selective laser melting process. Int J Simul Model 2011;10(3):113–21.

[32] Li C, Fu C, Guo Y, Fang F. A multiscale modeling approach for fast prediction of part distortion in selective laser melting. J Mater Process Technol 2016;229:703–12.

[33] Hodge N, Ferencz R, Solberg J. Implementation of a thermomechanical model for the simulation of selective laser melting. Comput Mech 2014;54(1):33–51.

[34] Schilp J, Seidel C, Krauss H, Weirather J. Investigations on temperature fields during laser beam melting by means of process monitoring and multiscale process modelling. Adv Mech Eng 2014;6:217584.

[35] Gouge M, Denlinger E, Irwin J, Li C, Michaleris P. Experimental validation of thermo-mechanical part-scale modeling for laser powder bed fusion processes. Addit Manuf 2019.

[36] Papadakis L, Loizou A, Risse J, Schrage J. Numerical computation of component shape distortion manufactured by selective laser melting. Procedia Cirp 2014;18:90–5.

[37] Zaeh MF, Branner G. Investigations on residual stresses and deformations in selective laser melting. Prod Eng 2010;4(1):35–45.

[38] Zhang W, Tong M, Harrison NM. Resolution, energy and time dependency on layer scaling in finite element modelling of laser beam powder bed fusion additive manufacturing. Addit Manuf 2019;28:610–20.

[39] Yavari MR, Cole KD, Rao P. Thermal modeling in metal additive manufacturing using graph theory. J Manuf Sci Eng 2019;141(7):071007.

[40] Peng H, Ghasri-Khouzani M, Gong S, Attardo R, Ostiguy P, Gatrell BA, et al. Fast prediction of thermal distortion in metal powder bed fusion additive manufacturing: Part 1, a thermal circuit network model. Addit Manuf 2018;22:852–68.

[41] Ganeriwala R, Zohdi TI. A coupled discrete element-finite difference model of selective laser sintering. Granul Matter 2016;18(2):1–15.

[42] McMillan M, Leary M, Brandt M. Computationally efficient finite difference method for metal additive manufacturing: A reduced-order DFAM tool applied to SLM. Mater Des 2017;132:226–43.

[43] Promoppatum P, Yao S-C, Pistorius PC, Rollett AD, Coutts PJ, Lia F, et al. Numerical modeling and experimental validation of thermal history and microstructure for additive manufacturing of an Inconel 718 product. Prog Addit Manuf 2018;3(1):15–32.

[44] Chen Q, Zhao Y, Strayer S, Zhao Y, Aoyagi K, Koizumi Y, et al. Elucidating the effect of preheating temperature on melt pool morphology variation in Inconel 718 laser powder bed fusion via simulation and experiment. Addit Manuf 2021;37:101642.
[45] Tran H-C, Lo Y-L, Le T-N, Lau AK-T, Lin H-Y. Multi-scale simulation approach for identifying optimal parameters for fabrication ofhigh-density Inconel 718 parts using selective laser melting. Rapid Prototyp J 2021.
[46] Denlinger ER, Irwin J, Michaleris P. Thermomechanical modeling of additive manufacturing large parts. J Manuf Sci Eng 2014;136(6).
[47] Li C, Gouge MF, Denlinger ER, Irwin JE, Michaleris P. Estimation of part-to-powder heat losses as surface convection in laser powder bed fusion. Addit Manuf 2019;26:258–69.
[48] Thijs L, Verhaeghe F, Craeghs T, Humbeeck JV, Kruth J-P. A study of the microstructural evolution during selective laser melting of Ti–6Al–4V. Acta Mater 2010;58(9):3303–12.
[49] Naraghi MH. Energy dynamics of green buildings. Linus Learning; 2020.
[50] Tveito A, Winther R. Introduction to partial differential equations: A computational approach. Berlin, Heidelberg: Springer; 2005.
[51] Wang Q, et al. Part-scale thermal evolution and post-process distortion of Inconel-718 builds fabricated by laser powder bed fusion. J Manuf Process 2022.
[52] Aermica makes 4026: Development of distortion prediction and compensation methods for metal powder-bed AM. https://www.americamakes.us/portfolio/4026-development-distortion-prediction-compensation-methods-metal-powder-bed/.
[53] Palm WJ. System dynamics. 3rd ed. New York, NY: McGraw-Hill; 2013.
[54] Loeb AL. Thermal conductivity: VIII, a theory of thermal conductivity of porous materials. J Am Ceram Soc 1954;37(2):96–9.
[55] Smith DS, Alzina A, Bourret J, Nait-Ali B, Pennec F, Tessier-Doyen N, et al. Thermal conductivity of porous materials. J Mater Res 2013;28(17):2260–72.
[56] Rombouts M, Froyen L, Gusarov A, Bentefour EH, Glorieux C. Photopyroelectric measurement of thermal conductivity of metallic powders. J Appl Phys 2005;97(2):024905.
[57] Wei LC, Ehrlich LE, Powell-Palm MJ, Montgomery C, Beuth J, Malen JA. Thermal conductivity of metal powders for powder bed additive manufacturing. Addit Manuf 2018;21:201–8.
[58] Alkahari MR, Furumoto T, Ueda T, Hosokawa A, Tanaka R, Abdul Aziz MS. Thermal conductivity of metal powder and consolidated material fabricated via selective laser melting. In: Emerging technology in precision engineering XIV. Key engineering materials, vol. 523, Trans Tech Publications Ltd; 2012, p. 244–9.